ACS Electrochemistry

pubs.acs.org/electrochem
Article

Evaluating the Pressure Dependence of Charge Transport in Composite Cathodes for Solid-State Batteries

Johannes Schubert,* Philip Minnmann, Sascha Kremer, Janis K. Eckhardt, Anja Bielefeld, and Jürgen Janek*

Cite This: ACS Electrochem. 2026, 2, 1583−1597
Read Online

ABSTRACT: Solid-state batteries (SSBs) are seen as a promising advancement of conventional lithium-ion batteries that use liquid electrolytes. Yet, their current reliance on operation under high stack pressures is a key challenge for wide-scale application. In this context, the composite cathode microstructure is of crucial importance as interface contact between the active material and solid electrolyte as well as charge transport pathways must remain intact under low-pressure operation. In this work, we evaluate the electrochemical charge transport properties of composite cathodes consisting of $LiNi_{0.82}Mn_{0.07}Co_{0.11}O_2$ and Li_6PS_5Cl at different stack pressures. By using solid electrolytes with different particle size distributions, we investigate how a change in the composite microstructure affects the pressure dependence of effective electronic and ionic conductivities. The effective electronic conductivity is found to be highly sensitive to pressure. Even though the effective ionic conductivity is less sensitive to pressure, it also diminishes when the stack pressure is decreased and approaches practically relevant values. A reduced solid electrolyte particle size leads to higher effective ionic conductivity, but it has no influence on the pressure dependence as such. This demonstrates the need for solid electrolytes that not only feature an optimized particle size distribution but also tailored mechanical properties. Considering the strong pressure dependence of electronic charge transport, SSB cells with and without conductive carbon were tested at different stack pressures. The results highlight the benefits of an electronically conductive additive during low stack pressure operation.

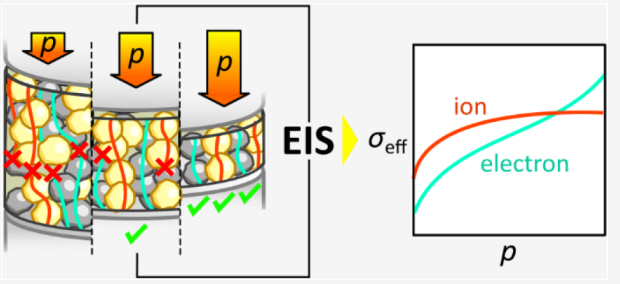

KEYWORDS: *charge transport, solid-state batteries, stack pressure, impedance spectroscopy, sulfide*

INTRODUCTION

Solid-state batteries (SSBs) have emerged as a viable advancement of conventional liquid electrolyte-based lithium-ion batteries (LIBs) for electric vehicles and other mobile applications. By substituting the flammable liquid electrolyte with an inorganic solid electrolyte (SE) higher safety is expected. In addition, SSBs also offer a potentially higher energy density as a solid-state separator is considered an enabler of the lithium metal anode.[1,2]

In recent years, the growing interest in SSBs has led to the development of a variety of SEs with high ionic conductivities and enhanced electrochemical stability.[3−5] At the same time a better understanding of the fundamental processes occurring in the cell facilitated the design of improved cell components, *e.g.* electrodes with optimized microstructures or functional interlayers.[6−10] As a result, the cycling performance of SSBs has quickly progressed and cells that feature a high cycling stability and energy densities surpassing those of LIBs have been demonstrated in laboratory studies.[11] However, these SSB cells typically operate at stack pressures of often 50 MPa and more which is well above the low pressures exerted on conventional LIBs.[12] The still unsatisfactory performance at low stack pressures is one of the major obstacles preventing the use of SSBs with inorganic SEs in practical applications so far. And one of the critical and open questions is whether anode and cathode have different stack pressure requirements.

Ideally, a lithium metal anode is utilized for the sake of high specific capacity and high energy density. For the lithium metal anode, high stack pressure is required to maintain intimate interfacial contact toward the SE separator. Although too high pressure can facilitate dendrite propagation and creep, insufficient stack pressure will lead to current constriction at the limited contact areas, causing non-uniform plating and stripping and eventually failure of the cell.[13−15] While the advantages of high fabrication pressures have been demonstrated for the cathode, the stack pressure requirements and in particular the minimum acceptable pressure are less clear.[16,17] A

Received: April 7, 2026
Revised: May 22, 2026
Accepted: May 22, 2026
Published: June 1, 2026

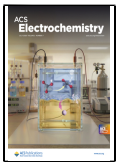

https://doi.org/10.1021/acselectrochem.6c00144
ACS Electrochem. 2026, 2, 1583−1597

wide range of pressure between 1 and 80 MPa has been used in previous studies, leaving room for improvement.[12,18]

In SSBs, the cathode is a particle composite that consists of the cathode active material (CAM), the SE and usually a carbon-based conductive additive. Even though low-strain CAMs are under active development, typical intercalation-type CAMs such as transition metal oxides undergo volume changes of several percent during (de-)lithiation. Furthermore, these occur anisotropically along the different crystallographic orientations.[8,19−22] This causes local contact loss between CAM and SE and leads to a reduction of the electrochemically active interface area and a decreased CAM utilization.[23,24] Moreover, the formation of voids will result in more tortuous electronic and ionic charge transport pathways, and hence, an increased cell impedance.[25] The blockage of ionic charge transport pathways is particularly detrimental when the CAM fraction is high as continuous ionic transport pathways are reduced in number and length. Maintaining a high stack pressure during cycling can mitigate these chemo-mechanical degradation phenomena of the composite microstructure, and therefore, significantly improve cycling performance.[26] To date, several tens of MPa are typically applied, if the cathode is the primary object of investigation.[12] As mentioned above, such high stack pressure is prohibitive for practical application.

Sulfide-based SEs are currently seen as one of the most promising inorganic catholyte materials. They do not only offer high ionic conductivities, *e.g.* up to 12 mS cm^{-1} for $Li_{5.5}PS_{4.5}Cl_{1.5}$ at 298 K, but are also relatively malleable at ambient temperature.[3,27−29] Compared to transition metal oxides, the sulfide-based SEs exhibit a considerably higher elasticity and plasticity. A relatively dense pellet with a residual porosity of 10−20% can easily be formed when a powder mixture of SE and CAM materials is densified even at ambient temperature.[30−33]

The transport properties of sulfide-based SEs have already been investigated under different pressure conditions.[34−39] Schneider *et al.* measured the ionic conductivity of Li_7SiPS_8 with two different particle size distributions at pressures from several MPa to more than 1.5 GPa. While increasing the pressure initially led to enhanced ionic conductivity, pressures above 500 MPa resulted in a compressed molar volume and thereby reduced lithium ion mobility which caused a reduction in conductivity.[35] Moreover, the influence of the homogeneity of the particle size distribution on the densification properties was shown in a recent study.[39] Cronau *et al.* demonstrated that the crystallinity of SE particles influences the pressure dependence of the ionic conductivity, which was attributed to different degrees of pressure-induced sintering during the initial densification of the powder.[36]

The ionic conductivity of a pre-densified Li_6PS_5Cl (LPSCl) pellet has been shown to be weakly stack pressure dependent when an intimate contact toward the current collector is assured.[17] In agreement with these results, in an SSB cell consisting of a Li−In alloy anode and composite cathode with $LiNi_{0.80}Co_{0.15}Al_{0.05}O_2$, no capacity improvement was observed upon stack pressure increase from 5 to 125 MPa during cycling with a low C-rate. In contrast to the stack pressure, a low fabrication pressure was found to result in worse cycling performance.[17] Although using the same SE as catholyte, Naik *et al.* observed a decreasing capacity below a threshold of approx. 10−20 MPa. Importantly, this effect became more pronounced when the C-rate was increased from 0.1C to 1C. This was attributed to limited solid−solid contact, which was supported by simulations of the local Li concentration in the composite cathode at different stack pressures.[18]

Altering the cathode composition and catholyte SE, Gao *et al.* demonstrated the importance of sufficient ionic conductivity of the catholyte to maximize the CAM utilization at a stack pressure of 2 MPa. In addition, maximized CAM utilization required careful adjustment of the conductive carbon content.[40] Although these results show that the performance of SSBs can be improved at low stack pressures, the high SE and carbon content in the cathode as well as operation at elevated temperature during cycling in that study come with trade-offs. A lower CAM content results in a lower energy density and high operating temperatures may be impractical for many applications. For sulfides, high carbon contents were shown to facilitate SE oxidation at the SE|carbon interface as electron transport toward the current collector is promoted.[41,42] Improving electronic and ionic charge transport while maintaining a low SE and carbon content is therefore essential to enhance the cathode performance.

The influence of the microstructure on the charge transport properties of composite cathodes was shown in several studies.[33,43−47] The evaluation of effective electronic and ionic conductivities by electrochemical impedance spectroscopy (EIS) revealed that volume fractions of CAM and SE should be carefully balanced to achieve optimal electronic and ionic charge transport.[46] Recent work has also demonstrated the crucial role of CAM and SE particle size distributions.[45,47,48] Small SE particles can fill voids between CAM particles and thereby provide additional ionic conduction pathways leading to a lower ionic tortuosity.[33] In a similar way, increased fabrication pressures were shown to result in less pore space and intimate interparticle contact, and therefore, a reduced cathode impedance.[16] Bae Song *et al.* determined the electronic and ionic tortuosity factors of $LiNi_{0.88}Co_{0.11}Mn_{0.01}O_2$/LPSCl composites at 3, 7, and 20 MPa.[49] Even though their findings showed an impact of stack pressure on the effective ionic and particularly electronic conductivity, the influence of stack pressure on charge transport and its correlation with the composite microstructure has yet received limited attention.

In this study, we evaluate electronic and ionic charge transport properties of composite cathodes as a function of microstructure and stack pressure. By measuring effective conductivities in a wide pressure range between 2 and 375 MPa, we aim to gain a better understanding of the (electrochemo-)mechanical behavior of the composite under pressure. We use composites without a conductive additive consisting of sieved LPSCl powders with different particle size distributions (D_{50} = 4−25 μm) as catholyte and $LiNi_{0.82}Co_{0.11}Mn_{0.07}O_2$ (NCM) to investigate the interplay of microstructure and pressure and its effect on the charge transport. Furthermore, the sieved SE powders are compared to a milled SE powder to assess the potential impact of milling on the SE particles and how this may affect the properties of the composite. Based on these results, we compare the cycling performance of SSBs with 3 wt % and without conductive carbon at different stack pressures. We show, that effective electronic and ionic conductivity both decline upon stack pressure reduction, with the effective electronic conductivity being particularly sensitive to pressure. The SE particle size influences the effective conductivities, but it does not impact the pressure dependence as such. At low stack pressures conductive carbon is found to be highly beneficial, as it compensates for the low electronic conductivity of the CAM network.

https://doi.org/10.1021/acselectrochem.6c00144
ACS Electrochem. 2026, 2, 1583−1597

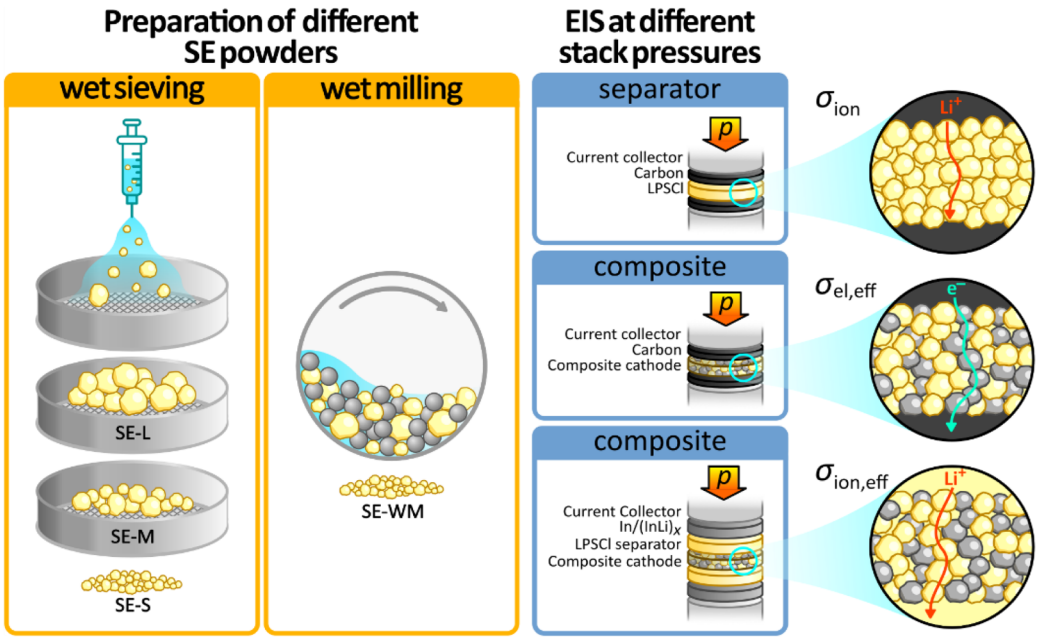

Figure 1. Schematic illustration of powder preparation and employed symmetric cell configurations. Three powder fractions (denoted as SE-L, SE-M and SE-S) were obtained by solvent-assisted sieving, and one powder fraction (SE-WM) was obtained by solvent-assisted milling. EIS was performed at different stack pressures using three different multi-layer cell stacks to determine σ_{ion} of the pure SE materials as well as $\sigma_{el,eff}$ and $\sigma_{ion,eff}$ of NCM:LPSCl composites.

EXPERIMENTAL SECTION

Materials

A wet sieving approach was employed to obtain three SE powders with differing particle size distributions. Li_6PS_5Cl (NEI Corporation) and o-xylene (anhydrous, Sigma-Aldrich) were mixed in a powder-to-solvent weight ratio of 1:10. To separate agglomerated SE particles, the suspension was dispersed for 15 min using a magnetic stirrer and a handheld ultrasonicator (Hielscher). Subsequently, the suspension was taken up with a syringe and vigorously pressed through a sieve with a mesh size of 45 μm. The residual material on the mesh was collected and went through the same treatment for a second time. The material which passed through the mesh was then again sieved with a mesh size of 25 μm and, in a final step, with a mesh size of 10 μm. The procedure is sketched in Figure 1. The suspensions were centrifuged and the solvent was decanted. Finally, all powders were dried for 12 h at 200 °C under dynamic vacuum in a drying oven (Büchi). In the following, the powders which passed the mesh sizes of 45 μm, 25 μm, and 10 μm are denoted as SE-L, SE-M, and SE-S, respectively.

A fourth powder (SE-WM) was prepared in a wet milling process. For this, a mixture of 15 g LPSCl, 45 mL *o*-xylene and 70 g zirconia milling media (1 mm diameter) was filled into an 80 mL zirconia jar and subjected to planetary ball milling (Pulverisette 7, Fritsch) for three 20 min periods. After each period of milling at a rotational speed of 500 rpm, the jar was allowed to cool down for 10 min. Lastly, the solvent was removed, and the powder was dried in the same manner as for the sieved samples.

Particle Size Analysis

The particle size distribution of the SE powders was obtained from SEM images. Secondary electron images were acquired with a pixel size of 93 nm at a voltage of 2 kV using a GeminiSEM 560 high resolution scanning electron microscope (Zeiss). Particles were identified using the *Segment Anything Model* which is a pre-trained deep learning model designed for instance segmentation of any type of object.[50] In addition to the segmentation performed on the original high-resolution SEM images, segmentation was also performed on smaller subsections of the images (1/12 of the image dimension along both axes) to ensure the detection of small particles. The segmented original image and the segmented subsections were subsequently merged, and the area-based particle size distribution was calculated using *Scikit-Image*.[51]

Preparation of Symmetric Cells

For preparation of cathode composites with different SE particle size distributions, $LiNi_{0.82}Co_{0.11}Mn_{0.07}O_2$ (D_{50} = 3−5 μm, MSE Supplies) and each of the prepared LPSCl powders were mixed with a weight ratio of 70:30 using a mini vibrating mill (Pulverisette 23, Fritsch).[52] Three zirconia balls (5 mm diameter) were added per 100 mg of material, and the mixture was agitated for 30 min with an oscillation frequency of 15 Hz.

Symmetric cell configurations were assembled in a CompreCell 12DP (rhd Instruments), which is an airtight cell setup specifically designed for electrochemical testing at adjustable stack pressures. In this cell, a cavity with a diameter of 12 mm is formed in a polyetherether ketone (PEEK) sleeve between two hard-metal pistons. Three cell configurations were used to measure a) the ionic conductivity σ_{ion} of the different LPSCl powders, b) the effective electronic conductivity $\sigma_{el,eff}$ and c) the effective ionic conductivity $\sigma_{ion,eff}$ of the composite (see Figure 1).

a) For measurement of the ionic conductivity of the LPSCl powders, a carbon-coated aluminum foil disc (PI-KEM) with a diameter of 11.8 mm was placed in the cavity and 75 mg LPSCl powder were added. The powder was slightly compressed by hand resulting in a flat surface, a second disc was added and the stack was densified at 375 MPa and room temperature for 3 min.
b) The symmetric cells for measuring the effective electronic conductivity $\sigma_{el,eff}$ of the cathode composite were prepared in the same way, but with the composite in the cavity. Due to the higher density of the composite compared to the pure SE powder, 100 mg composite powder were used.
c) For measuring the effective ionic conductivity $\sigma_{ion,eff}$ of the composite, an electron blocking symmetric cell configuration was used. To obtain a sufficiently stable pellet for further handling, 100 mg of the composite powder was slightly compressed by hand within the cavity in the CompreCell. Two separator layers were formed by addition of 100 mg of untreated LPSCl, *i.e.*, as delivered by the supplier, on both sides of the composite layer and subsequent densification of the stack at 260 MPa for 3 min. An indium foil disc (100 μm thickness,

https://doi.org/10.1021/acselectrochem.6c00144
ACS Electrochem. 2026, 2, 1583−1597

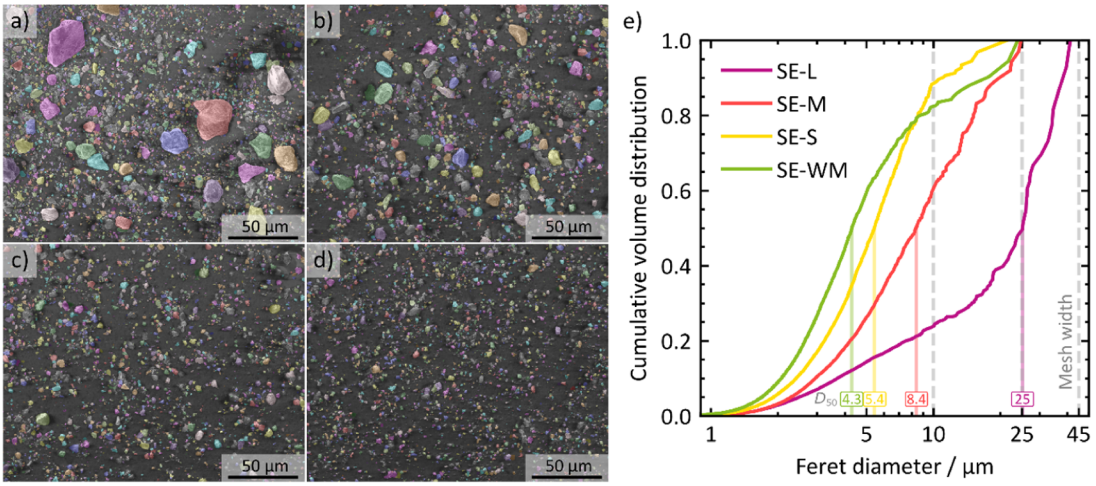

Figure 2. Colored SEM images of SE powders and results of particle size analysis. SEM images are sections of larger high-resolution images (see Figure S1) which contain 15,000−25,000 particles. a) SE-L, b) SE-M, c) SE-S; d) SE-WM. e) Cumulative particle size distributions as obtained by deep-learning assisted analysis of SEM images. Grey dashed lines indicate the mesh widths of the employed sieves, solid lines mark the D_{50}-values corresponding to the powders.

11.8 mm diameter, ChemPur) and a lithium foil disc (100 μm thickness, 6 mm, China Energy Lithium) were then placed on both separator layers. To provide time for the formation of the In/$(\text{In Li})_x$ two phase equilibrium, a 30 min waiting period followed during which a pressure of 50 MPa was applied. Finally, the stack was densified at 375 MPa for 3 min. To evaluate the impedance contribution of the In/$(\text{In Li})_x$ electrode and separator layers, a second electron blocking cell configuration was prepared. In comparison to the first electron blocking cell configuration, the composite layer was omitted and the In/$(\text{InLi})_x$ layers were pressed on one separator layer of twice the thickness.

Preparation of SSB Cells

SSB cells were assembled in an in-house developed setup.[53] First, 60 mg of untreated LPSCl were filled into a PEEK sleeve with a diameter of 10 mm and densified between two steel pistons with a hand press. Subsequently, 18 mg composite material was homogeneously distributed on the separator layer and the stack was densified at 375 MPa for 3 min. Two composites without and with conductive additive were tested. In addition to the composite containing SE-WM, which was also used in the symmetric cell configurations, the second composite was prepared in an identical way except that 3 wt % carbon nanofibers (100 nm; 20−200 μm, Sigma-Aldrich) were added prior to mixing the composite. Finally, an indium disc (9 mm diameter) and a lithium disc (6 mm diameter) were placed on the separator layer.

Electrochemical Characterization

Electrochemical impedance spectroscopy (EIS) of symmetric cells was carried out with a Neisys potentiostat (Novocontrol Technologies) with an excitation amplitude of 42 mV and at 25 °C. For measurements of SE pellets and for measurements of composite pellets, the impedance was recorded between 10 MHz and 1 Hz and between 10 MHz and 10 mHz, respectively. A CompreDrive laboratory-press (rhd Instruments) was used to vary the stack pressure after every impedance measurement. Starting at an initial pressure of 2 MPa, the pressure was stepwise increased to maximum pressures of 150, 375, and 150 MPa and subsequently stepwise decreased back to 2 MPa after reaching the maximum value in three successive cycles.

SSB cells were cycled with a BCS-800 (Biologic) between 2.6 and 4.3 V vs. Li^+/Li at different C-rates (1C = 200 mA g_{CAM}^{-1}). All experiments were conducted at 25 °C and with a stack pressure of 5, 75, or 125 MPa, which was monitored by an in-house built pressure frame. Prior to cycling a pressure of 50 MPa was applied for 3 h.

Focused Ion Beam-Scanning Electron Microscopy

To visualize the microstructure of the composites, cross sections of the pellets were prepared using a XEIA3 focused ion beam-scanning electron microscope (FIB-SEM, Tescan) equipped with a Xe-plasma ion source. All sample transfers were conducted under vacuum or inert Ar-atmosphere using a *VCT* transfer module (Leica).

RESULTS

Analysis of the Particle Size Distribution and Composite Microstructure

To obtain LPSCl powders with different particle size distributions, the untreated LPSCl powder was separated into three different fractions, SE-L ($d \leq 45$ μm), SE-M ($d \leq 25$ μm) and SE-S ($d \leq 10$ μm) in a wet sieving process (see Figure 1). Compared to milling, sieving allows improved control of the aimed particle size distribution and has the advantage that morphological or structural changes induced by mechanical stresses can be excluded.[54,55] A degradation of the SE due to the solvent treatment was not observed. SEM images of the resulting powder fractions are depicted in Figure 2a−c and confirm that particles larger than the used mesh size can effectively be removed by sieving. However, sieving cannot completely separate smaller from larger particles when the powders undergo consecutive sieving steps with decreasing mesh sizes. While this is partly caused by the irregular shape of the particles, *i.e.*, elongated particles cannot pass the sieve, the main cause is an insufficient deagglomeration of particle clusters during the sieving process. We like to note that initial attempts to sieve the dry SE powders resulted in significantly lower yields, as strong agitation of the sieves rather led to a formation of particle agglomerates than separate particles. For comparison, a fourth powder (SE-WM) was prepared via ball milling, which exhibits particle sizes comparable to those of sample SE-S (see Figure 2d).

To quantify the particle size distribution, the maximum Feret diameter of the particles, *i.e.*, the longest length between two points on the particle outline, and the equivalent diameter, *i.e.*, the diameter of a circle with the same area, were extracted from the SEM images. With respect to the three-dimensional composite microstructure, the volume distribution is more meaningful compared to number and area distribution (which

https://doi.org/10.1021/acselectrochem.6c00144
ACS Electrochem. 2026, 2, 1583−1597

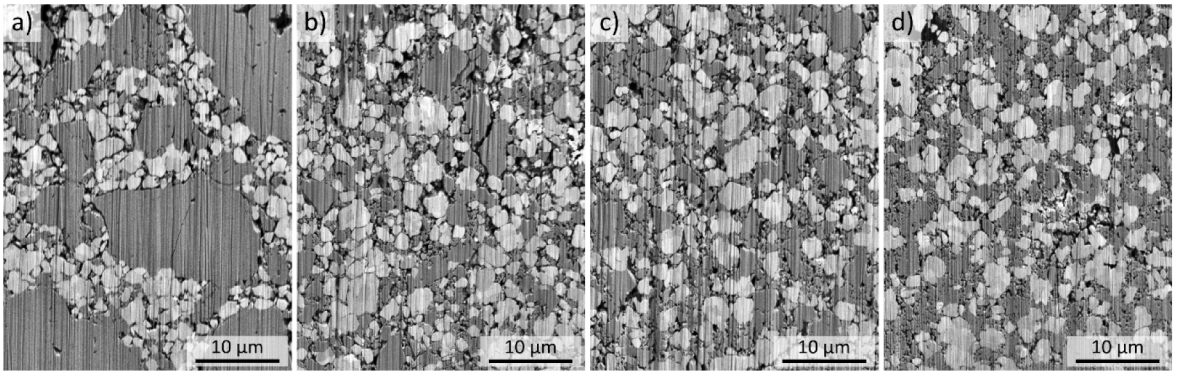

Figure 3. FIB-SEM images of NCM:LPSCl cathode composites with different LPSCl particle sizes. NCM particles appear bright, whereas LPSCl particles appear dark. a) SE-L, b) SE-M, c) SE-S; d) SE-WM.

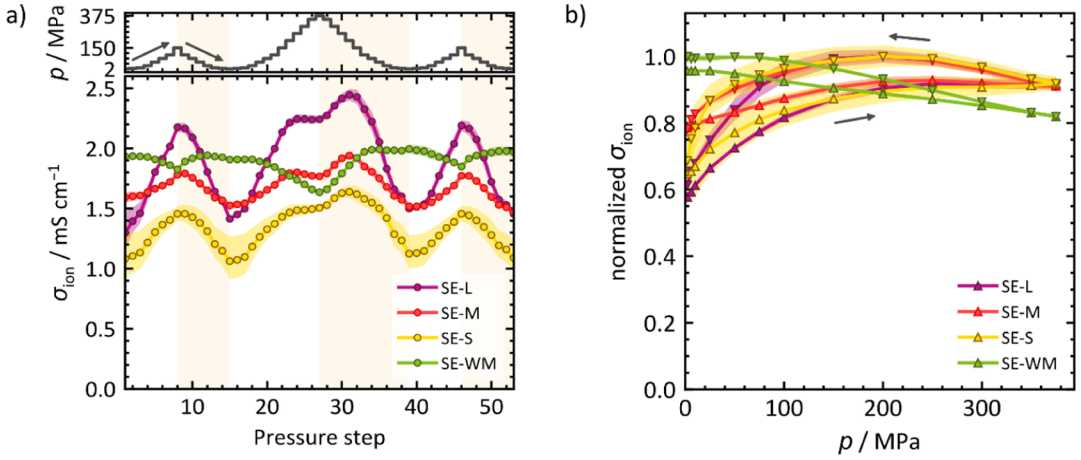

Figure 4. a) Evolution of σ_{ion} of SE pellets measured with (carbon-CC|SE|carbon-CC) cells for different stack pressures (impedance spectra are depicted in Figure S6). The dark gray line depicts the stack pressure for each pressure step. The colored lines are the average of 2−3 samples and shaded areas indicate minimum and maximum values of these samples. b) Evolution of σ_{ion} for the second pressure cycle (pressure steps 15−39) normalized to the maximum value. Increasing and decreasing pressure are indicated by right-pointing and left-pointing arrows, respectively.

can however directly be extracted from two-dimensional SEM images, see Figure S2) and was therefore calculated using the equivalent diameter and assuming spherical particles. Figure 2e shows the cumulative particle size volume distribution as obtained by analysis of the SEM images. For SE-L and SE-M the D_{50} values of 25 μm and 8.4 μm, respectively, are considerably larger compared to 5.4 μm and 4.3 μm for SE-S and SE-WM. Despite smaller D_{50} values for SE-S and SE-WM, the data indicate the presence of some particles larger than 10 μm. This, however, is mostly caused by particle agglomerates in the SEM images which are falsely identified as a single particle.

To evaluate the influence of the SE particle size on the composite microstructure, cross sections of the pelletized composites were imaged by FIB-SEM (see Figure 3). In addition, we provide phase fractions and chord length distributions extracted from the cross sections as quantitative microstructural descriptors in the Supplementary Information (see Figures S3−S5). For SE-L, particles larger than 10 μm are visible (confirmed by a higher fraction of longer chords) which cause a clustering of CAM particles in the surrounding space. Since the fraction of small SE particles is low, void spaces between individual CAM particles (D_{50} = 3−5 μm) are not filled by the SE leading to a high residual porosity within the CAM network. With decreasing SE particle size clustering of CAM particles becomes less pronounced which results in more homogeneous phase distribution. In particular, for SE-S and SE-WM, a homogeneous distribution of phases is observed. Due to the comparable microstructures for SE-S and SE-WM, differences of the electrochemical and mechanical properties of these cathode composites may be governed more by the catholyte than microstructural features. This simplifies the evaluation of the impact of wet milling on the SE properties.

Pressure Dependence of the Ionic Conductivity of the SE

To evaluate the influence of pressure on σ_{ion} of the SE, pressure dependent EIS was measured for pellets consisting solely of the SE. In previous studies, combined EIS and thickness measurements during the densification of SE powders have been used for complementary investigation of compression mechanics and ionic conductivity of sulfides.[35,39,56] However, those studies were limited to cell configurations containing only the SE as constituent. In contrast, we performed stack pressure dependent measurements after densification as this facilitates the use of multi-layered cell configurations. These, consequently, enable the use of established methods for electronic and ionic charge transport characterization of composite cathodes.[46,47] A wide pressure range of 2 MPa to 375 MPa is selected, which covers the stack pressure regime typically used for press cell operation and extends to pressures often used for powder densification during cell preparation. While the lower pressure range (< 80 MPa) is therefore directly relevant for cell operation and the determined conductivities may allow conclusions on cell performance, the

https://doi.org/10.1021/acselectrochem.6c00144
ACS Electrochem. 2026, 2, 1583−1597

higher pressure range can offer further insights into the fundamental relationship between charge transport, mechanical properties and densification behavior.

Figure 4a shows σ_{ion} in three consecutive pressure cycles (a pressure cycle consists of one ramp with increasing pressure and one ramp with decreasing pressure) for the four SE powders. For the sieved powders (SE-L, SE-M, SE-S), in the first pressure cycle σ_{ion} increases monotonically until the maximum pressure of 150 MPa is reached. Upon pressure release, σ_{ion} decreases to the initial value following a similar profile. This can be explained by elastic deformation of the SE particles upon external pressure which reduces void space and forms SE-SE interparticle contacts. With respect to the latter, the stack pressure is considered to be particular effective in reducing current constriction as voids at the rough particle surface could vanish. When the stack pressure is raised to 375 MPa, σ_{ion} approaches a plateau as further densification above a relative density of 92−94% is limited (see Figure S9). Interestingly, upon pressure release from 375 MPa, σ_{ion} shows a hysteresis which may be explained by a delayed relaxation of the microstructure, *e.g.* voids which slowly reopen, or reversible particle rearrangements. We note that dedicated modeling of the composite microstructure upon pressure application and relaxation—also including the elastic and plastic properties of the SE—may provide further insights into the observed trends of σ_{ion}, but are beyond the scope of this study.

Comparing the first and the last pressure cycle no increase of σ_{ion} is observed. This confirms that after the initial densification no further particle rearrangement and irreversible densification occurs during the course of the measurement.

Apart from elastic deformation of the SE particles two other effects may contribute to a decrease of the impedance at increasing stack pressure:

(1) A contact resistance between the SE pellet and the current collector at low pressures: This has been observed by Doux *et al.* in measurements of σ_{ion} with ion blocking metal current collectors.[17] The authors were able to minimize this additional contribution by the use of a carbon layer between metal and SE pellet since the soft carbon can adapt to the rough pellet surface. In agreement with these results, comparative measurements conducted without a carbon layer showed a high impedance at pressures below 50 MPa that likely arises from an insufficient SE-current collector contact at the pellet surface (see Figure S7). While the resistances of samples without and with carbon layer converge above 50 MPa, the resistance of the sample with carbon layer is decreased by approximately 80% at 2 MPa. Without carbon layer the impedance spectrum shows an additional high-frequency contribution at the low pressures, which is not visible for the sample with carbon layer. We therefore expect the contact resistance to be negligible. A quantification of the residual contact resistance is, however, not possible, as its contribution to the impedance spectrum is not fully resolved. A small residual contact resistance cannot be fully excluded and may introduce minor uncertainty into the reported conductivity values at low pressures.

(2) A reduction of the pellet thickness l: An accurate measurement of l during pressure application was not possible. Although an increase of the stack pressure will result in a slight decrease of l, we assumed l to be constant to calculate σ_{ion} according to eq 1:

$$\sigma_{ion} = \frac{l}{R_{ion} \cdot A} \quad (1)$$

with the ionic resistance R_{ion} and the cell area A. As an indicator of the thickness change, the steps driven by the stepper motor of the CompreDrive were recorded (see Figure S8). Based on these results, we estimate the change of l compared to the initial l to be below 10% and a minor contribution to the observed pressure dependence of σ_{ion} (see Figure S9). This slight overestimation of σ_{ion} is similar for all samples and therefore does not change the general trend observed for the influence of the SE particle size.

Generally, we observed that smaller SE particles lead to a lower σ_{ion}. We attribute this to the grain boundary resistance at the SE-SE interparticle contacts which are prevalent in pellets consisting of fine SE powders.[33,35,57] To further assess the influence of particle size, for the second pressure cycle, σ_{ion} was normalized to its maximum value and plotted against the pressure (see Figure 4b). For SE-S to SE-L, this yields similar data with a difference of 20−40% between the minimum value of 2 MPa and the maximum value of 375 MPa for the sieved samples. The influence of the particle size on the pressure dependence of σ_{ion} as such is therefore negligible.

In contrast to the sieved powders, the milled powder (SE-WM) shows a distinctly different behavior. Although SE-WM has the smallest median particle size of the four powders and the highest contribution of SE-SE interparticle contact resistance can be assumed, at low stack pressures, σ_{ion} is the highest. When the pressure exceeds 25 MPa, σ_{ion} decreases and a hysteresis is only weakly pronounced. We attribute this to a lower degree of crystallinity of the milled powder which is confirmed by a slight reflection broadening in X-ray diffractograms (see Figure S10). Structural changes, such as defects, and particularly an amorphization of the particle surface can lead to a reduced interface resistance or changed mechanical properties. As a consequence, cold sintering of particles during the initial densification of the powder may be facilitated resulting in stronger irreversible interparticle bonding. Differences in the cold sintering properties of amorphous, glass ceramic and microcrystalline thiophosphates have also been reported by Cronau *et al.*[36]

The reason for decreasing σ_{ion} with increasing pressure is unclear and will be subject of future work. Generally, σ_{ion} can be affected when the local pressure, *i.e.,* strain, is sufficiently high to result in a distortion of the local lattice and an influence on Li^+ mobility.[58,59] The impact of high pressure on σ_{ion} of sulfide SEs has rarely been studied but a visible decrease of σ_{ion} has not been observed below at least 100 MPa for highly crystalline samples.[35,37] Due to residual voids and poor interparticle contact, the pressure dependence of σ_{ion} at lower pressures may rather be dominated by microstructural changes. We like to note that one of three SE-WM samples showed lower values for σ_{ion} below 10 MPa (see Figure S11). We attribute this to a poor contact between sample surface and current collector due to a kinked, *i.e.*, non-planar, carbon-coated aluminum foil disc or a stuck piston. This sample was, therefore, assumed to be an outlier and is not included in Figure 4.

Pressure Dependence of the Effective Electronic Conductivity of Cathode Composites

From separator pellets, we proceeded to composites that contain the various SE powders and NCM. As shown by the influence of a soft carbon layer between SE pellet and hard-metal current collectors at low stack pressures, the contact resistance between

https://doi.org/10.1021/acselectrochem.6c00144
ACS Electrochem. 2026, 2, 1583−1597

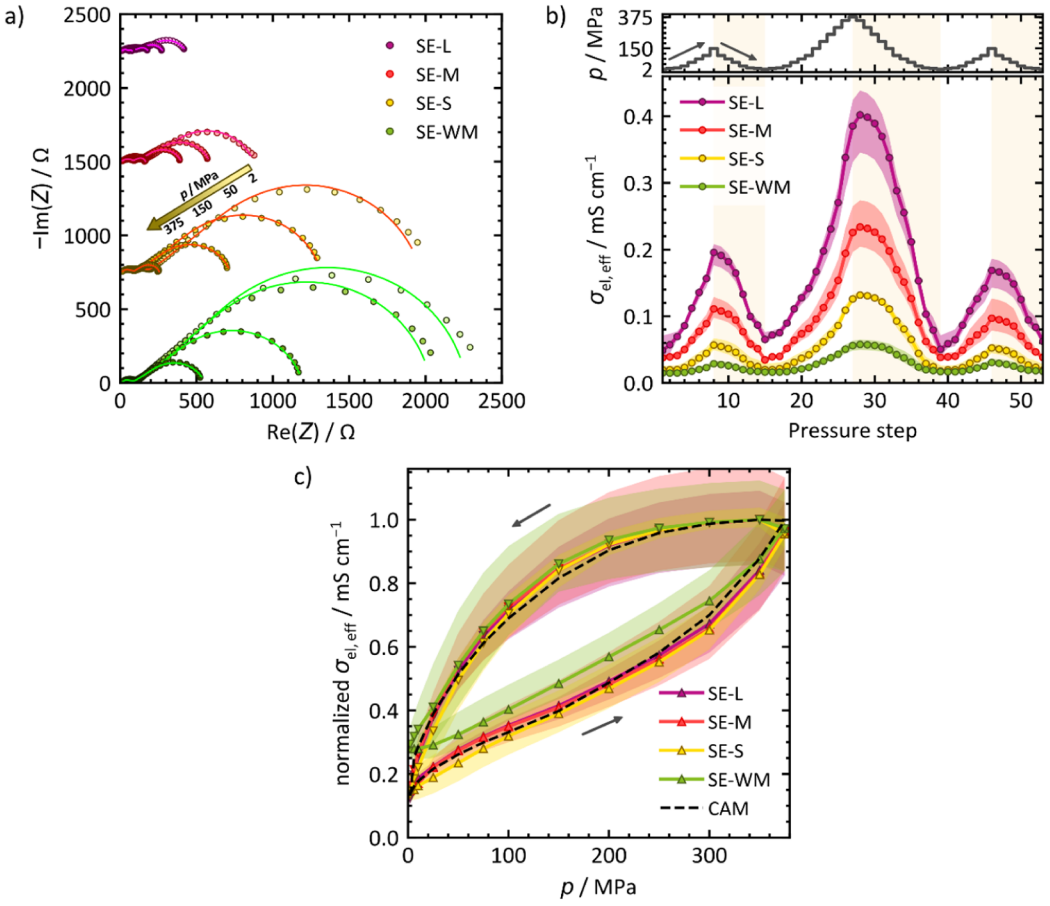

Figure 5. a) Impedance spectra of ion blocking (carbon-CC|composite|carbon-CC) cells and corresponding fits. Depicted are exemplary spectra recorded during increasing pressure of the second pressure cycle. b) Evolution of $\sigma_{el,eff}$ of the composites for different stack pressures. The gray line depicts the stack pressure for each pressure step. Lines are the average of 2−3 samples and shaded areas indicate minimum and maximum values of these samples. c) Evolution of $\sigma_{el,eff}$ for the second pressure cycle (pressure steps 15−39) normalized to the maximum value (the evolution of σ_{el} of the CAM is depicted in Figure S14). Increasing and decreasing pressure are indicated by right-pointing and left-pointing arrows, respectively.

sample and current collectors can have a significant impact on the impedance and must either be minimized by an appropriate cell setup or, if possible, discerned in the impedance spectrum. Especially in the case of hard materials, such as NCM, a rough sample surface, and hence, a higher contact resistance may be assumed as the particles cannot deform and adapt to an equally hard current collector surface. In the case of sintered NCM pellets the effectiveness of a carbon layer to reduce the contact resistance toward the current collector surface has already been demonstrated by Kuo *et al.*[60] Therefore, for determination of the effective electronic conductivity $\sigma_{el,eff}$ of the cathode composites, impedance spectra were recorded using an ion blocking cell configuration with a carbon layer placed between the composite pellet and the hard-metal pistons. The significant reduction of the impedance at low stack pressures (see Figure S12) confirms the beneficial effect of the soft carbon layer to mitigate the contact resistance in the case of pure SE materials and composites.

Figure 5a shows the impedance spectra of ion blocking cells at four different stack pressures during the second pressure cycle in Nyquist representation. All spectra exhibit a smaller semicircle at higher frequencies and a larger semicircle at lower frequencies which originate from the concurrent conduction of electrons and ions in the CAM and SE phase. When the stack pressure is increased, the impedance decreases, however, the shape of the spectra does not change. This indicates a continuous enhancement of electronic and ionic conduction, as opposed to an abrupt change in conduction pathways for either charge carrier, which would likely result in an alteration of the shape.

For fitting of the impedance spectra, a T-type transmission line model (TLM) is employed since its two-path structure represents the electronic conduction in the CAM phase, parallel to the ionic conduction in the SE phase, with both phases sharing a charge transfer boundary (see Figure S13). T-type TLMs have been used multiple times to describe the impedance of composite cathodes.[33,46,47,54,61,62] They refer to the symmetrical termination of the conduction pathways, *i.e.*, terminations at the electronic conduction pathway for an ion blocking configuration, necessary to appropriately represent the symmetric cell configuration. The electronic pathway consists of a serial connection of resistors corresponding to intra-particle bulk conduction and a R-CPE unit representing interparticle charge-transfer through the CAM-CAM interface. A serial connection of resistors is used to model the ionic pathway. Since the charge transfer resistance of fully lithiated NCM is high and non-faradaic behavior can be assumed, the CAM-SE interface impedance is represented by a CPE.

For consecutive pressure cycles, the effective electronic conductivity $\sigma_{el,eff}$ of all composites shows a similar profile (see Figure 5b). Upon pressure increase to 150 MPa, $\sigma_{el,eff}$ increases strongly and monotonously. Stepwise pressure decrease leads to a reduction of $\sigma_{el,eff}$ and finally a reversible drop to the initial

https://doi.org/10.1021/acselectrochem.6c00144
ACS Electrochem. 2026, 2, 1583−1597

value at 2 MPa. In the second pressure cycle the strong increase continues above 150 MPa and results in a fivefold increase of $\sigma_{el,eff}$ at 375 MPa. Importantly, $\sigma_{el,eff}$ does not reach a plateau at high pressures, which is in distinct contrast to σ_{ion} of the SE pellets and can be explained by the substantially different mechanical properties of CAM and SE. Due to the higher malleability, SE particles are expected, to some extent, to adapt to the surface of neighboring SE particles resulting in a growing interparticle contact area, and therefore, additional conduction pathways. While the leveling of σ_{ion} of the SE pellets indicates no considerable further improvement of interparticle contact at pressures above 150 MPa, the low elasticity of the CAM does not allow for conformal contact between neighboring CAM particles even at high pressures.[31] As a consequence, increasing pressure likely results in a continuous increase of locally confined contact spots over the whole pressure range. These results are in agreement with observations by Miß *et al.* who measured an increase of σ_{el} upon pressurization of NCM pellets.[63] When the pressure is decreased, $\sigma_{el,eff}$ remains high but reverts to the initial value when the pressure approaches 2 MPa. The resulting hysteresis of $\sigma_{el,eff}$ is significantly more pronounced compared to the SE pellets. Similarly, as for the SE pellets, full reversibility of $\sigma_{el,eff}$ upon consecutive pressure application and release implies that further irreversible particle rearrangement and plastic deformation do not take place during the experiment.

Since the electronic pathway of the TLM includes impedance elements corresponding to bulk transport in CAM particles and transport across the CAM-CAM interface, fitting of the impedance allows to separate the pressure dependence of both processes (see Figure S15). The interfacial resistance is found to be the dominant factor contributing to the electronic resistance and dominates the overall pressure dependence of electronic conduction, which is reasonable as it relies on the contact area between CAM particles. In addition, resistive residual compounds on the particle surface originating from synthesis or storage as well as electronically insulating protective coatings can impair charge transport at the CAM-CAM contact.[64,65] Sufficient pressure between neighboring CAM particles can enable local penetration of these layers resulting in preferential conduction pathways. In accordance with that, the observed strong pressure dependence of $\sigma_{el,eff}$ may be caused by a boron-rich layer present on the surface of the employed CAM (see Figure S16). In contrast, the electronic bulk resistance shows virtually no dependence of pressure and is at least one order of magnitude lower than the interfacial resistance.

We identified the SE particle size distribution as a crucial factor influencing effective charge transport and subsequently the performance of the cathode. Small particles can fill voids between CAM particles and, overall, lead to a more homogeneous phase distribution and increased CAM-SE interface areas, which significantly influences charge transport and performance. In line with previous findings, the determined values for $\sigma_{el,eff}$ demonstrate a strong influence of the SE particle size on $\sigma_{el,eff}$ with a clearly visible reduction of $\sigma_{el,eff}$ when finer SE powders are used.[33,46] This can be attributed to the increasing number of small SE particles which are distributed within the CAM network and lead to more tortuous electronic conduction pathways.[43,44]

As CAM and SE do not only have different conducting properties but also distinctly different mechanical properties, the mechanical properties of the cathode are as well influenced by the composite microstructure. As described above, the SE particle size distribution influences the distribution of phases and porosity. Consequently, a changed interplay of the constituents, *e.g.* a changed interparticle contact caused by a finely dispersed continuous SE phase within the CAM network, could result in a changed microstructural response upon increased pressure. For the different composites this results in a different pressure dependence of charge transport itself. Therefore, for comparison of the pressure dependence, $\sigma_{el,eff}$ was normalized to its maximum value for all samples (see Figure 5c).

Plotting the normalized value of $\sigma_{el,eff}$ against the pressure yields almost identical curve profiles independent of the SE particle size. To evaluate the influence of the SE itself, the same measurement protocol was performed for a pure CAM pellet and the normalized electronic conductivity σ_{el} was calculated (dashed lines). The corresponding profile agrees well with those of the composites with sieved SEs. While the pressure dependence of $\sigma_{el,eff}$ in the composites with sieved powders is completely independent of the SE, the composite with the milled powder shows slightly higher values particularly at low pressures. Consistent with the assumed improved cold sintering properties of SE-WM, in the latter case, the SE may provide a stabilizing matrix for the CAM particle network which helps in maintaining contact between CAM particles.

Pressure Dependence of the Effective Ionic Conductivity of Cathode Composites

For the determination of the effective ionic conductivity $\sigma_{ion,eff}$ of the composites, an electron blocking symmetric cell configuration was used. In this configuration, the composite layer is on both sides confined by a separator and an $In/(InLi)_x$ layer serving as lithium reservoir. The contribution of the $In/(InLi)_x$|SE interface to the impedance typically overlaps with the signal originating from the composite, and hence, proper fitting of the impedance spectra requires a thorough evaluation of that contribution at different stack pressures. For this, the impedance of a separator layer sandwiched between two $In/(InLi)_x$ layers was measured as a function of the pressure separately (see Figure S17). The spectra were then fitted with an R-(R-CPE) equivalent circuit corresponding to the resistance of the separator layer and the $In/(InLi)_x$|SE interface.

The $In/(InLi)_x$|SE interface contribution was found to be particularly affected by cell preparation. When In and Li foils were stacked on the separator layer and the measurements were conducted after a waiting time of 30 min without further treatment, the impedance showed a significant dependence of the pressure (see Figure 6). Moreover, in the first pressure steps, poor spectrum quality, likely caused by a non-conformal $In/(InLi)_x$|SE contact, prevented fitting and quantification of the interface resistance at pressures below 50 MPa. Subsequent pressure application, however, led to a decreasing impedance which becomes particular apparent after the cell stack was pressurized at 375 MPa. Since the $In/(InLi)_x$|SE interface resistance remained largely unaffected by the following pressure release, plastic deformation of the alloy under sufficiently high pressure can be assumed to result in an improved and mostly irreversible intimate interfacial contact.

Based on these results, comparative experiments were conducted for which the cell stack including the $In/(InLi)_x$ layers was pressurized (30 min at 50 MPa followed by 3 min at 375 MPa) prior to the measurement. Following this protocol, the interface resistance shows only a weakly pronounced pressure dependence with considerably reduced values at low pressures, and importantly, a high reproducibility among three different cells. We therefore suggest pressurization of the In/

https://doi.org/10.1021/acselectrochem.6c00144
ACS Electrochem. 2026, 2, 1583−1597

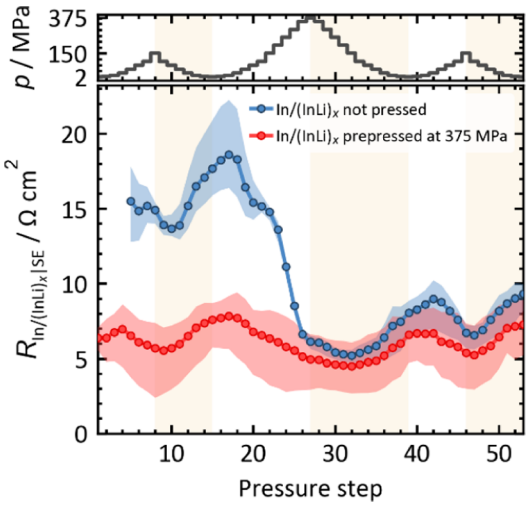

Figure 6. Resistance of the In/$(InLi)_x$|SE interface at different stack pressures for (In/$(InLi)_x$|SE|In/$(InLi)_x$) cells without prior pressurization of the In/$(InLi)_x$ layer (blue) and with prior pressurization of the In/$(InLi)_x$ layer at 375 MPa (red). Lines are the average of three samples and shaded areas indicate minimum and maximum values of these samples. When the cell is not pressurized beforehand, poor spectrum quality prevents fitting with a R-(R-CPE) equivalent circuit below 50 MPa. Note that the fit value was divided by two to account for the symmetric configuration.

$(InLi)_x$ layers prior to impedance measurements of symmetrical cell configurations with a lithium reservoir to minimize interfering contributions to the impedance signal of the composite. These findings are also applicable to SSB cells and are consistent with recent results by Kissel *et al.* who reported a lower absolute impedance contribution as well as lower variations between individual cells when the In/$(InLi)_x$ layer was pressed at 375 MPa.[52]

Impedance spectra of the electron blocking cells including the composite at selected stack pressures are depicted in Figure 7a. As in case of the ion blocking cells all spectra show two semicircles originating from electronic and ionic charge transport in the composite as well as the overlapping contribution of the In/$(InLi)_x$|SE interface. For fitting of the spectra, the above-described T-type TLM was adapted to the modified cell configuration by changing the termination to the ionic conduction path. To account for the separator and the In/$(InLi)_x$|SE interface, a R-(R-CPE) circuit was connected in series with the terminals of the TLM. Boundaries for the fitting parameters of the R-CPE element were specified based on the results of the (In/$(InLi)_x$|SE|In/$(InLi)_x$) cells.

The overall trend for $\sigma_{ion,eff}$ upon consecutive pressure increase and decrease resembles that of σ_{ion} of the pure SE samples (see Figure 7b). The microstructural response of the SE phase in the composite under mechanical stress is, therefore, most likely comparable to that of SE pellets. Elastic deformation of SE particles leads to an increasing number of ionic conduction pathways particularly at pressures below 100−150 MPa. This reversible densification of the SE phase is reasonable as the hard CAM particles can be assumed to transfer stress to softer SE particles. Similar behavior of σ_{ion} and $\sigma_{ion,eff}$ was also observed upon pressure decrease, and both show a hysteresis. In contrast to σ_{ion} of the SE pellets, however, the normalized value of $\sigma_{ion,eff}$ is slightly lower at low pressures and continues to moderately increase up to 375 MPa (see Figure 7c), which may be explained by a non-uniform stress distribution within the composite. As demonstrated by Ohashi *et al.* for a composite consisting of two constituents with differing Young's moduli, the stress transferred to the softer constituent will be lower than the stress applied on the composite.[66] Consequently, some regions of the SE phase may be shielded by surrounding CAM particles from the applied pressure and the formation of ionic conduction pathways will be impeded. While a certain pressure may be sufficient to maximize σ_{ion} in pure SE samples, in the composite, higher pressures will be required to enhance ionic conduction specifically in these low stress regions resulting in a moderate increase of $\sigma_{ion,eff}$ even at very high pressures. A notable implication is that, compared to the pure SE, ionic conduction in a composite cathode is not only hindered due to tortuous pathways introduced by the CAM phase but also to some extent by charge transport bottlenecks caused by locally insufficient pressure.

With decreasing SE particle size, a trend toward higher $\sigma_{ion,eff}$ was observed. As described above, this is in good agreement with previous reports and is attributed to the reduction of porosity and a more homogeneous phase distribution.[33,47] Interestingly, despite comparable particle sizes, SE-WM shows a considerably higher $\sigma_{ion,eff}$ than SE-S. Similar to $\sigma_{el,eff}$ an influence of the SE powder on the pressure dependence of $\sigma_{ion,eff}$, which may be assumed due to a changed microstructure, was not observed. This is remarkable as the pressure dependence of σ_{ion} for the pure SE-WM samples was found to be distinctly different compared to that of the sieved powders. These differences were attributed to different cold sintering properties of the SE. However, the similar pressure dependence of $\sigma_{ion,eff}$ in the composite for sieved and milled SE powders suggests that these altered SE properties have no substantial effect in the composite.

Clearly, the malleability of sulfide SEs provides advantages in achieving favorable microstructures for composite cathodes. Yet, our results show that charge transport is considerably impeded at pressures approaching application-relevant values compared to high pressures typically applied to press cells in laboratory studies. While smaller SE particles generally enable less tortuous conduction pathways, and hence, enhance ionic conduction, an additional beneficial impact specifically at low pressures was not observed. Designing composites with optimized SE particle size distributions is therefore necessary but a mere reduction of the SE particle size is most probably not sufficient to resolve the unsatisfactory performance of sulfide-based SSBs close to atmospheric pressure conditions.

We like to note that SE particles which are significantly smaller than CAM particles, CAM fractions higher than the here used 70 wt % as well as improved mixing or densification strategies may influence the distribution of CAM and SE phase. Consequently, this may also influence the mechanical interplay of both phases and thereby change the pressure dependence of charge transport as such. However, our results show no differences of the pressure dependence of $\sigma_{ion,eff}$ when the D_{50} value of the SE powder is reduced from 25 μm to 5 μm, despite substantially more homogeneous phase distributions. Therefore, we also expect a similar pressure dependence of $\sigma_{ion,eff}$ when *e.g.* the SE particle size is further reduced. Apart from these factors, the pressure dependence of charge transport may also be influenced by the densification procedure, such as densification at elevated temperatures, which could lead to improved SE interparticle contact. Nonetheless, in addition to high σ_{ion} and an optimized particle size distribution of the SE, improved low-pressure performance will require SEs with more beneficial mechanical properties, *i.e.*, higher plasticity and elasticity. In this regard, SEs with optimized mechanical properties such as highly

https://doi.org/10.1021/acselectrochem.6c00144
ACS Electrochem. 2026, 2, 1583−1597

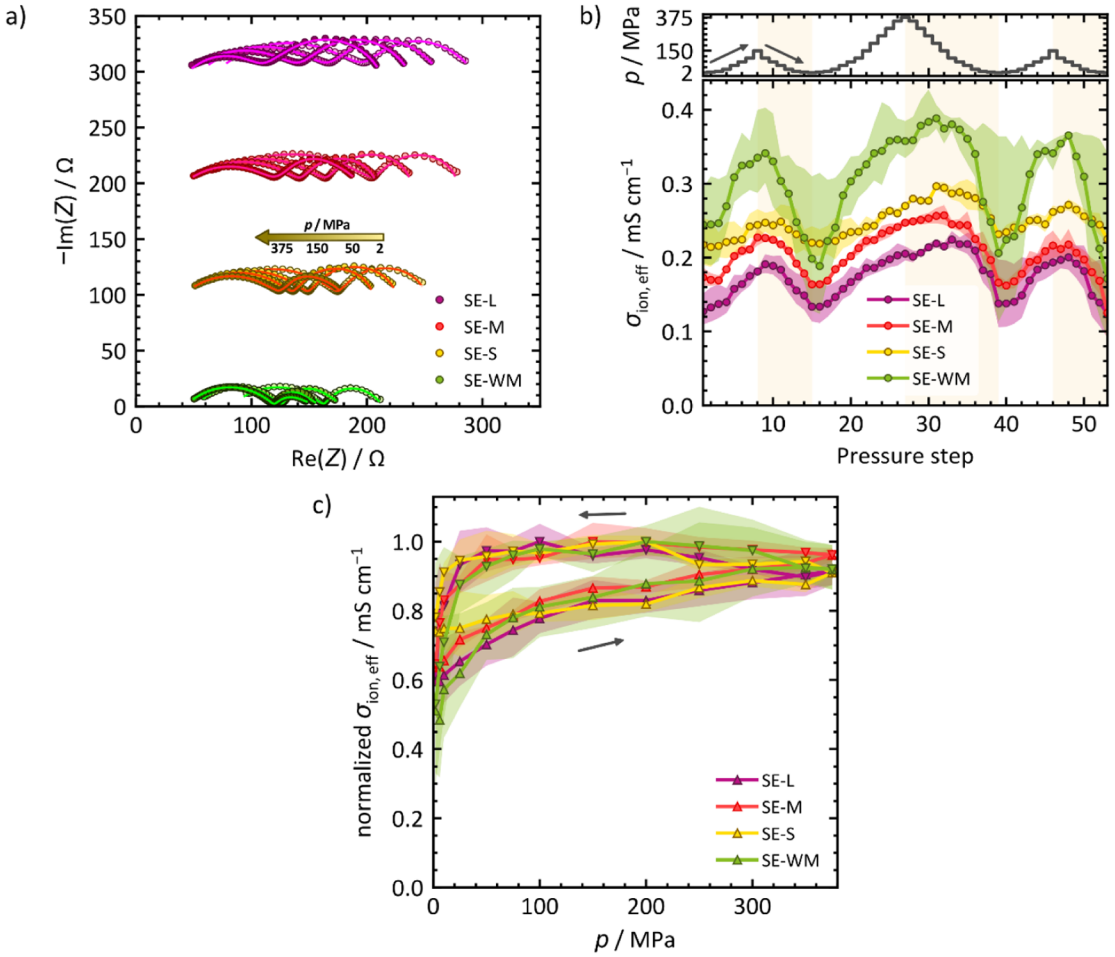

Figure 7. a) Impedance spectra of electron blocking $(In/(InLi)_x|SE|composite|SE|In/(InLi)_x)$ cells and corresponding fits. Depicted are exemplary spectra recorded during increasing pressure of second pressure cycle. b) $\sigma_{ion,eff}$ of the composites for different stack pressures. The gray line depicts the stack pressure for each pressure step. Lines are the average of 2−3 samples and shaded areas indicate minimum and maximum values of these samples. c) $\sigma_{ion,eff}$ for the second pressure cycle (pressure steps 15−39) normalized to the maximum value. Increasing and decreasing pressure are indicated by right-pointing and left-pointing arrows, respectively.

deformable glassy SEs, as reported recently, appear as a promising option.[67−69] Considering the variety of potential catholytes and additional microstructural factors affecting the mechanical properties of the composite, our results highlight the need for more systematic investigations on the pressure dependence of effective charge transport in composites with different types of SEs. Even though $\sigma_{ion,eff}$ is a crucial property, our results demonstrate that $\sigma_{el,eff}$ is strongly affected by the stack pressure as well. This is in line with results of Bae Song *et al.* who reported a stronger increase of $\sigma_{el,eff}$ compared to $\sigma_{ion,eff}$ when the stack pressure was increased from 3 to 20 MPa.[49] In contrast to $\sigma_{ion,eff}$, $\sigma_{el,eff}$ can relatively easily be enhanced by adding conductive additives to the composite. While carbon is therefore usually added to the composite, its influence on the performance of SSB cells at different stack pressures has, to the authors knowledge, not yet been systematically studied.

Impact of Conductive Carbon on the Performance at Low Stack Pressures

To demonstrate the influence of the pressure dependent charge transport, and specifically that of $\sigma_{el,eff}$, on the performance of SSB cells, cells were cycled at stack pressures of 5, 75, and 125 MPa. A stack pressure of 75 MPa is in the range of 50 MPa to 80 MPa often applied for cycling of press cells, while 5 and 125 MPa were chosen as lower and upper bounds, respectively, to evaluate the performance under different pressure conditions.[12]

The effective conductivities measured with symmetric cell configurations indicate a strong impact of pressure on $\sigma_{el,eff}$. Consequently, the introduction of electronically conductive additives to the cathode composite can significantly enhance electronic charge transport especially when the electronic conductivity of the CAM network itself is low, *i.e.*, at low stack pressures. Cycling experiments were, therefore, conducted with and without carbon nanofibers. Randau *et al.* reported a percolation threshold of around 3 wt % of carbon fibers at which further addition of the conductive additive will not result in a further decrease of the electronic tortuosity.[70] In addition, first cycle charge and discharge curves indicated increased degradation when the carbon fiber content surpassed 2−3 wt %. Based on these results we chose a mass fraction of 3 wt % to ensure the formation of a percolating network which can provide electronic conduction pathways independent of the applied stack pressure. Despite the relatively high carbon content, initial cycle charge and discharge curves showed no signs of degradation (see Figure S19). SE-WM was used as catholyte as it not only provides the highest $\sigma_{ion,eff}$ but the small SE particles also block electronic conduction pathways. Therefore, the beneficial effect of the electronic additive should be the

https://doi.org/10.1021/acselectrochem.6c00144
ACS Electrochem. 2026, 2, 1583−1597

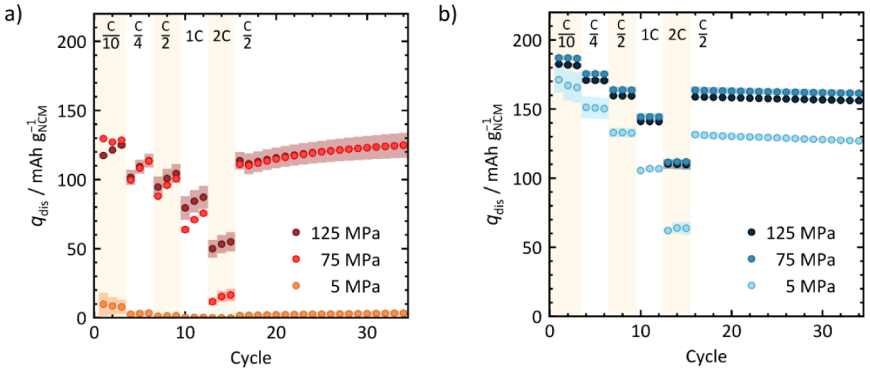

Figure 8. Electrochemical cycling performance of SSB cells. Circles are the average of two cells and shaded areas indicate minimum and maximum values of these cells. a) Cathode without carbon nanofibers. b) Cathode with 3 wt % carbon nanofibers. SE-WM was used as catholyte. The areal capacity is 3.2 mAh cm^{-2}.

strongest resulting in a distinct difference between cells with and without carbon fibers. Moreover, unlike sieving, milling represents a commercially more viable route for further reducing the SE particle size and the milled powder is of the highest practical relevance.

At a stack pressure of 5 MPa, cells containing no carbon in the cathode do not exceed an initial discharge capacity of approx. 20 mAh g^{-1} even at a low C-rate of 0.1C (see Figure 8a). For higher C-rates the discharge capacity quickly drops to 0. At high stack pressures of 75 and 125 MPa, the initial discharge capacity is similar and with approx. 130 mAh g^{-1} significantly higher than at 5 MPa. However, this value is considerably lower than the theoretical capacity of 200 mAh g^{-1}, indicating a poor CAM utilization even under high pressure. For increasing C-rates, kinetic limitations led to rapidly diminishing capacities, which was less pronounced at the highest pressure. These results are consistent with the enhanced electronic and ionic charge transport observed under increased stack pressures in symmetric cell configurations. However, during cycling the CAM undergoes volume changes which lead to contact loss at the CAM|SE interface, thereby decreasing the electrochemically active interface area. Moreover, these volume changes may also result in deteriorated electronic charge transport as contact points between CAM particles vanish. These aspects cannot be accounted for in symmetric cell configurations, which do not allow for (de-)lithiation of the CAM, but can be expected to have a strong influence on the performance at different stack pressures.

Even though the performance is also influenced by the pressure dependence of contact loss and ionic charge transport, enhancing electronic charge transport proves to be particularly beneficial at low pressure (see Figure 8b). Introducing carbon into the cathode significantly increases the discharge capacities for all stack pressures. The most distinct difference compared to cells without carbon is observed at a low stack pressure of 5 MPa. At 5 MPa a high initial capacity of around 170 mAh g^{-1} is reached, only slightly lower than that of cells cycled at 75 and 125 MPa. Although the low stack pressure causes a more pronounced capacity decrease at higher C-rates, the capacity still surpasses 60 mAh g^{-1} at 2C.

We like to note that achieving these capacities at 5 MPa required storing the cells temporarily at approx. 50 MPa prior to cycling. The storing period under pressure likely promotes the formation of a uniform interface between anode and separator with a decreased interface impedance as also demonstrated with the symmetric $(In/(InLi)_x|SE|In/(InLi)_x)$ configuration. While this led to a significant improvement of the cycling performance of cells with carbon fibers, it had no impact on the performance of cells without carbon fibers.

We therefore attribute the diverging performance to the presence of a carbon fiber network, which provides high effective electronic conductivity even at low pressures. The carbon compensates for the low electronic conductivity of the CAM network caused by a smaller number of CAM-CAM contact points. This beneficial effect may be even more important when the integrity of the CAM network deteriorates due to volume changes and insufficient stack pressure and the number of contact points decreases further. If electronic charge transport is governed by the high carbon content and not the stack pressure, sufficient electronic conductivity can be assumed even at low pressures. Consequently, the improved rate capability at 75 and 125 MPa suggests that under low stack pressures insufficient ionic charge transport and CAM-SE contact limits SSB performance as well. Apart from providing additional electronic conduction pathways, the carbon fiber network may have an additional advantage with respect to preventing microstructural degradation. Carbon fibers enforce the microstructure mechanically and provide additional microstructural stability. Under low stack pressure this effect may be particularly beneficial.

In order to achieve competitive low-pressure operability, enhanced charge transport is required, in addition to materials with favorable mechanical properties offering optimized composite microstructures (see Figure 9). While $\sigma_{ion,eff}$ is indeed widely considered crucial, $\sigma_{el,eff}$ and σ_{el} of the CAM often appear to be overlooked. This must be taken into account as a reduction of the SE particle size has been identified as an effective strategy to increase $\sigma_{ion,eff}$. Smaller SE particles can block electronic conduction pathways and lead to decreased $\sigma_{el,eff}$. Similarly, modifications impeding electronic charge transport between CAM particles such as electronically insulating coatings may be particularly detrimental at low stack pressures. Although conductive carbon can be used to ensure electronic percolation, utilization of CAMs with intrinsically high σ_{el} would avoid carbon induced decomposition of the SE.[41] In addition, the effect of an intrinsically high σ_{el} will be further amplified if the CAM fraction is increased as required for cathodes with high energy density. Maintaining sufficiently high $\sigma_{el,eff}$ independent of stack pressure, therefore, is a prerequisite for satisfactory SSB performance.

https://doi.org/10.1021/acselectrochem.6c00144
ACS Electrochem. 2026, 2, 1583−1597

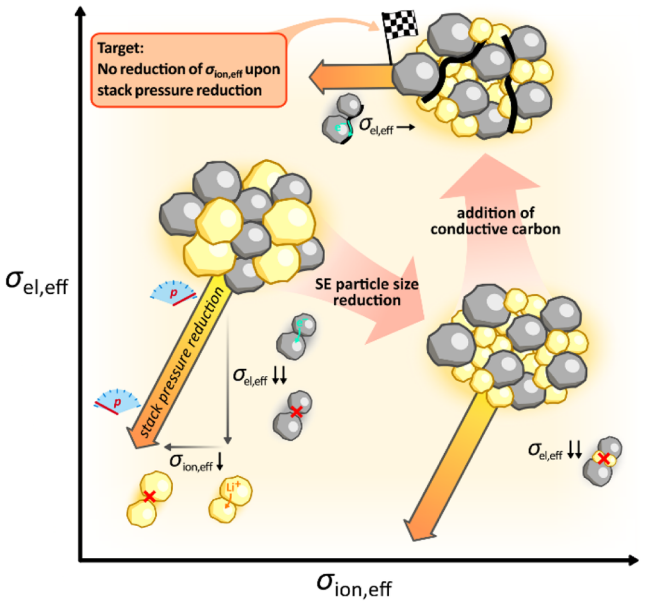

Figure 9. Schematic depiction of the influence of stack pressure on the effective electronic and ionic conductivities for different composites.

CONCLUSIONS

In this study, we investigate electronic and ionic charge transport in sulfide-based composite cathodes as a function of stack pressure. To evaluate the influence of the cathode microstructure on the pressure dependence of effective electronic and ionic conductivities, we employed LPSCl powders with different particle size distributions obtained by solvent-assisted sieving and milling. In the tested pressure range of 2 MPa to 375 MPa, $\sigma_{el,eff}$ is highly pressure dependent and increases steadily. In contrast, $\sigma_{ion,eff}$ shows no considerable increase at stack pressures typically reported for SSB cycling tests and above. Yet, compared to σ_{ion} in pure SE samples, $\sigma_{ion,eff}$ requires higher pressures to reach its maximum value. We attribute this to regions of the SE phase that are shielded by surrounding CAM particles from the applied pressure, resulting in locally insufficient pressure and impeded ionic charge transport. A pronounced decline of $\sigma_{ion,eff}$ at decreasing pressure approaching the practically relevant range, demonstrates the necessity of SEs with optimized mechanical properties. While smaller SE particles result in lower $\sigma_{el,eff}$ and higher $\sigma_{ion,eff}$, in line with recent reports, we cannot confirm an influence on the pressure dependence. Interestingly, we observe a significantly enhanced σ_{ion} of the milled SE at low pressures when tested as pure material. Although a similar effect is not visible in case of $\sigma_{ion,eff}$ of the composite, structural changes of the particle surface, which may be induced by milling, might influence the mechanical properties of the SE and should be a subject of future work. Motivated by the observed strong pressure dependence of $\sigma_{el,eff}$, we examined the performance of SSBs without and with conductive additive at different stack pressures. The capacity of cells with conductive additive is generally higher but the improvement is substantially higher for cells cycled at the lowest stack pressure of 5 MPa. This highlights the importance of a sufficient $\sigma_{el,eff}$ to improve the low pressure performance of SSBs. In addition to corroborating the crucial role of sufficiently high and balanced charge transport that has been demonstrated in previous work, our results show that measuring $\sigma_{el,eff}$ and $\sigma_{ion,eff}$ over a wide pressure range can provide valuable insights that enable the design of composite cathodes specifically optimized for low stack pressures.

ASSOCIATED CONTENT

Supporting Information

The Supporting Information is available free of charge at https://pubs.acs.org/doi/10.1021/acselectrochem.6c00144.

Additional experimental details and data, including SEM images of SE powders and extracted particle size distributions, segmented FIB-SEM cross-sections and extracted microstructural descriptors, impedance spectra and corresponding fitting parameters, as well as experimental details, X-ray diffractograms of SE powders, information on CAM composition, and voltage profiles of SSB cells (PDF)

AUTHOR INFORMATION

Corresponding Authors

Johannes Schubert − *Institute for Physical Chemistry, Justus-Liebig-University Giessen, Giessen 35392, Germany; Center for Materials Research, Justus-Liebig-University Giessen, Giessen 35392, Germany;* orcid.org/0009-0003-3148-6672; Email: johannes.schubert@phys.chemie.uni-giessen.de

Jürgen Janek − *Institute for Physical Chemistry, Justus-Liebig-University Giessen, Giessen 35392, Germany; Center for Materials Research, Justus-Liebig-University Giessen, Giessen 35392, Germany; BELLA, Institute for Nanotechnology, Karlsruhe Institute of Technology, Karlsruhe 76021, Germany;* orcid.org/0000-0002-9221-4756; Email: juergen.janek@phys.chemie.uni-giessen.de

Authors

Philip Minnmann − *Institute for Physical Chemistry, Justus-Liebig-University Giessen, Giessen 35392, Germany; Center for Materials Research, Justus-Liebig-University Giessen, Giessen 35392, Germany;* orcid.org/0000-0002-9646-0487

Sascha Kremer − *Institute for Physical Chemistry, Justus-Liebig-University Giessen, Giessen 35392, Germany; Center for Materials Research, Justus-Liebig-University Giessen, Giessen 35392, Germany;* orcid.org/0009-0009-3739-8749

Janis K. Eckhardt − *Center for Materials Research, Justus-Liebig-University Giessen, Giessen 35392, Germany;* orcid.org/0000-0002-2799-0599

Anja Bielefeld − *Institute for Physical Chemistry, Justus-Liebig-University Giessen, Giessen 35392, Germany; Center for Materials Research, Justus-Liebig-University Giessen, Giessen 35392, Germany;* orcid.org/0000-0003-2193-8375

Complete contact information is available at: https://pubs.acs.org/10.1021/acselectrochem.6c00144

Notes

The authors declare no competing financial interest.

ACKNOWLEDGMENTS

We acknowledge financial support within the FestBatt Cluster of Competence (BMBF, Bundesministerium für Bildung und Forschung) in the projects 03XP0430A, 03XP0433D, and 03XP0428E. We also acknowledge the German Research Foundation (DFG) POLiS Cluster of Excellence (Project ID

390874152) for financing the CompreDrive (RHD) device. J.K.E. and A.B. acknowledge financial support from the Hessian State Ministry of Higher Education, Research, and the Arts (HMWK).

REFERENCES

(1) Janek, J.; Zeier, W. G. A solid future for battery development. *Nat. Energy* **2016**, *1*, 16141.
(2) Janek, J.; Zeier, W. G. Challenges in speeding up solid-state battery development. *Nat. Energy* **2023**, *8*, 230−240.
(3) Kato, Y.; Hori, S.; Saito, T.; Suzuki, K.; Hirayama, M.; Mitsui, A.; Yonemura, M.; Iba, H.; Kanno, R. High-power all-solid-state batteries using sulfide superionic conductors. *Nat. Energy* **2016**, *1*, 16030.
(4) Zhou, L.; Minafra, N.; Zeier, W. G.; Nazar, L. F. Innovative Approaches to Li-Argyrodite Solid Electrolytes for All-Solid-State Lithium Batteries. *Acc. Chem. Res.* **2021**, *54*, 2717−2728.
(5) Kwak, H.; Kim, J.-S.; Han, D.; Kim, J. S.; Park, J.; Kwon, G.; Bak, S.-M.; Heo, U.; Park, C.; Lee, H.-W.; et al. Boosting the interfacial superionic conduction of halide solid electrolytes for all-solid-state batteries. *Nat. Commun.* **2023**, *14*, 2459.
(6) Sakuda, A.; Takeuchi, T.; Kobayashi, H. Electrode morphology in all-solid-state lithium secondary batteries consisting of LiNi1/3Co1/3Mn1/3O2 and Li2S-P2S5 solid electrolytes. *Solid State Ionics* **2016**, *285*, 112−117.
(7) Conforto, G.; Ruess, R.; Schröder, D.; Trevisanello, E.; Fantin, R.; Richter, F. H.; Janek, J. Editors' Choice—Quantification of the Impact of Chemo-Mechanical Degradation on the Performance and Cycling Stability of NCM-Based Cathodes in Solid-State Li-Ion Batteries. *J. Electrochem. Soc.* **2021**, *168*, 070546.
(8) Strauss, F.; de Biasi, L.; Kim, A.-Y.; Hertle, J.; Schweidler, S.; Janek, J.; Hartmann, P.; Brezesinski, T. Rational Design of Quasi-Zero-Strain NCM Cathode Materials for Minimizing Volume Change Effects in All-Solid-State Batteries. *ACS Mater. Lett.* **2020**, *2*, 84−88.
(9) Suzuki, N.; Yashiro, N.; Fujiki, S.; Omoda, R.; Shiratsuchi, T.; Watanabe, T.; Aihara, Y. Highly Cyclable All-Solid-State Battery with Deposition-Type Lithium Metal Anode Based on Thin Carbon Black Layer. *Adv. Energy Sustain. Res.* **2021**, *2* (11), 2100066.
(10) Wang, Z.; Xia, J.; Ji, X.; Liu, Y.; Zhang, J.; He, X.; Zhang, W.; Wan, H.; Wang, C. Lithium anode interlayer design for all-solid-state lithium-metal batteries. *Nat. Energy* **2024**, *9*, 251−262.
(11) Lee, Y.-G.; Fujiki, S.; Jung, C.; Suzuki, N.; Yashiro, N.; Omoda, R.; Ko, D.-S.; Shiratsuchi, T.; Sugimoto, T.; Ryu, S.; Ku, J. H.; Watanabe, T.; Park, Y.; Aihara, Y.; Im, D.; Han, I. T. High-energy long-cycling all-solid-state lithium metal batteries enabled by silver−carbon composite anodes. *Nat. Energy* **2020**, *5*, 299−308.
(12) Puls, S.; Nazmutdinova, E.; Kalyk, F.; Woolley, H. M.; Thomsen, J. F.; Cheng, Z.; Fauchier-Magnan, A.; Gautam, A.; Gockeln, M.; Ham, S.-Y.; et al. Benchmarking the reproducibility of all-solid-state battery cell performance. *Nat. Energy* **2024**, *9*, 1310−1320.
(13) Doux, J.-M.; Nguyen, H.; Tan, D. H. S.; Banerjee, A.; Wang, X.; Wu, E. A.; Jo, C.; Yang, H.; Meng, Y. S. Stack Pressure Considerations for Room-Temperature All-Solid-State Lithium Metal Batteries. *Adv. Energy Mater.* **2020**, *10* (1), 1903253.
(14) Kasemchainan, J.; Zekoll, S.; Spencer Jolly, D.; Ning, Z.; Hartley, G. O.; Marrow, J.; Bruce, P. G. Critical stripping current leads to dendrite formation on plating in lithium anode solid electrolyte cells. *Nat. Mater.* **2019**, *18*, 1105−1111.
(15) Krauskopf, T.; Richter, F. H.; Zeier, W. G.; Janek, J. Physicochemical Concepts of the Lithium Metal Anode in Solid-State Batteries. *Chem. Rev.* **2020**, *120*, 7745−7794.
(16) Nam, J. S.; To A Ran, W.; Lee, S. H.; Vuong, T. H. L.; Jo, H.; Lee, J.-H.; Hwang, S. M.; Kim, Y.-J. Densification and charge transport characterization of composite cathodes with single-crystalline LiNi0.8Co0.15Al0.05O2 for solid-state batteries. *Energy Storage Mater.* **2022**, *46*, 155−164.
(17) Doux, J.-M.; Yang, Y.; Tan, D. H. S.; Nguyen, H.; Wu, E. A.; Wang, X.; Banerjee, A.; Meng, Y. S. Pressure effects on sulfide electrolytes for all solid-state batteries. *J. Mater. Chem. A* **2020**, *8*, 5049−5055.
(18) Naik, K. G.; Jangid, M. K.; Vishnugopi, B. S.; Dasgupta, N. P.; Mukherjee, P. P. Interrogating the Role of Stack Pressure in Transport-Reaction Interaction in the Solid-State Battery Cathode. *Adv. Energy Mater.* **2024**, *15* (10), 2403360.
(19) Jung, S. H.; Kim, U.-H.; Kim, J.-H.; Jun, S.; Yoon, C. S.; Jung, Y. S.; Sun, Y.-K. Ni-Rich Layered Cathode Materials with Electrochemo-Mechanically Compliant Microstructures for All-Solid-State Li Batteries. *Adv. Energy Mater.* **2020**, *10*, 1903360.
(20) Park, G.-T.; Park, N.-Y.; Ryu, J.-H.; Sohn, S.-J.; Yu, T.-Y.; Kim, M.-C.; Baiju, S.; Kaghazchi, P.; Yoon, C. S.; Sun, Y.-K. Zero-strain Mn-rich layered cathode for sustainable and high-energy next-generation batteries. *Nat. Energy* **2025**, *10*, 1215−1225.
(21) Koerver, R.; Zhang, W.; De Biasi, L.; Schweidler, S.; Kondrakov, A. O.; Kolling, S.; Brezesinski, T.; Hartmann, P.; Zeier, W. G.; Janek, J. Chemo-mechanical expansion of lithium electrode materials − on the route to mechanically optimized all-solid-state batteries. *Energy Environ. Sci.* **2018**, *11*, 2142−2158.
(22) Minnmann, P.; Strauss, F.; Bielefeld, A.; Ruess, R.; Adelhelm, P.; Burkhardt, S.; Dreyer, S. L.; Trevisanello, E.; Ehrenberg, H.; Brezesinski, T.; et al. Designing Cathodes and Cathode Active Materials for Solid-State Batteries. *Adv. Energy Mater.* **2022**, *12*, 2201425.
(23) Koerver, R.; Aygün, I.; Leichtweiß, T.; Dietrich, C.; Zhang, W.; Binder, J. O.; Hartmann, P.; Zeier, W. G.; Janek, J. Capacity Fade in Solid-State Batteries: Interphase Formation and Chemomechanical Processes in Nickel-Rich Layered Oxide Cathodes and Lithium Thiophosphate Solid Electrolytes. *Chem. Mater.* **2017**, *29*, 5574−5582.
(24) Shi, T.; Zhang, Y.-Q.; Tu, Q.; Wang, Y.; Scott, M. C.; Ceder, G. Characterization of mechanical degradation in an all-solid-state battery cathode. *J. Mater. Chem. A* **2020**, *8*, 17399−17404.
(25) Sakka, Y.; Yamashige, H.; Watanabe, A.; Takeuchi, A.; Uesugi, M.; Uesugi, K.; Orikasa, Y. Pressure dependence on the three-dimensional structure of a composite electrode in an all-solid-state battery. *J. Mater. Chem. A* **2022**, *10*, 16602−16609.
(26) Hu, X.; Zhang, Z.; Zhang, X.; Wang, Y.; Yang, X.; Wang, X.; Fayena-Greenstein, M.; Yehezkel, H. A.; Langford, S.; Zhou, D.; Li, B.; Wang, G.; Aurbach, D. External-pressure−electrochemistry coupling in solid-state lithium metal batteries. *Nat. Rev. Mater.* **2024**, *9*, 305−320.
(27) Adeli, P.; Bazak, J. D.; Park, K. H.; Kochetkov, I.; Huq, A.; Goward, G. R.; Nazar, L. F. Boosting Solid-State Diffusivity and Conductivity in Lithium Superionic Argyrodites by Halide Substitution. *Angew. Chem. Int. Ed.* **2019**, *58*, 8681−8686.
(28) Famprikis, T.; Canepa, P.; Dawson, J. A.; Islam, M. S.; Masquelier, C. Fundamentals of inorganic solid-state electrolytes for batteries. *Nat. Mater.* **2019**, *18*, 1278−1291.
(29) Kamaya, N.; Homma, K.; Yamakawa, Y.; Hirayama, M.; Kanno, R.; Yonemura, M.; Kamiyama, T.; Kato, Y.; Hama, S.; Kawamoto, K.; Mitsui, A. A lithium superionic conductor. *Nat. Mater.* **2011**, *10*, 682−686.
(30) Papakyriakou, M.; Lu, M.; Liu, Y.; Liu, Z.; Chen, H.; McDowell, M. T.; Xia, S. Mechanical behavior of inorganic lithium-conducting solid electrolytes. *J. Power Sources* **2021**, *516*, 230672.
(31) Cheng, E. J.; Hong, K.; Taylor, N. J.; Choe, H.; Wolfenstine, J.; Sakamoto, J. Mechanical and physical properties of LiNi0.33Mn0.33Co0.33O2 (NMC). *J. Eur. Ceram. Soc.* **2017**, *37*, 3213−3217.
(32) Choi, S.; Jeon, M.; Ahn, J.; Jung, W. D.; Choi, S. M.; Kim, J.-S.; Lim, J.; Jang, Y.-J.; Jung, H.-G.; Lee, J.-H.; Sang, B.-I.; Kim, H. Quantitative Analysis of Microstructures and Reaction Interfaces on Composite Cathodes in All-Solid-State Batteries Using a Three-Dimensional Reconstruction Technique. *ACS Appl. Mater. Interfaces* **2018**, *10*, 23740−23747.
(33) Minnmann, P.; Schubert, J.; Kremer, S.; Rekers, R.; Burkhardt, S.; Ruess, R.; Bielefeld, A.; Richter, F. H.; Janek, J. Editors' Choice—Visualizing the Impact of the Composite Cathode Microstructure and Porosity on Solid-State Battery Performance. *J. Electrochem. Soc.* **2024**, *171*, 060514.

https://doi.org/10.1021/acselectrochem.6c00144
ACS Electrochem. 2026, 2, 1583−1597

(34) Kodama, M.; Komiyama, S.; Ohashi, A.; Horikawa, N.; Kawamura, K.; Hirai, S. High-pressure in situ X-ray computed tomography and numerical simulation of sulfide solid electrolyte. *J. Power Sources* **2020**, *462*, 228160.
(35) Schneider, C.; Schmidt, C. P.; Neumann, A.; Sadowski, M.; Harm, S.; Meier, C.; Albe, K.; Latz, A.; Wall, W. A. Effect of Particle Size and Pressure on the Transport Properties of the Fast Ion Conductor t-Li7SiPS8. *Adv. Energy Mater.* **2023**, *13*, 2203873.
(36) Cronau, M.; Szabo, M.; König, C.; Wassermann, T. B.; Roling, B. How to Measure a Reliable Ionic Conductivity? The Stack Pressure Dilemma of Microcrystalline Sulfide-Based Solid Electrolytes. *ACS Energy Lett.* **2021**, *6*, 3072−3077.
(37) Faka, V.; Agne, M. T.; Till, P.; Bernges, T.; Sadowski, M.; Gautam, A.; Albe, K.; Zeier, W. G. Pressure dependence of ionic conductivity in site disordered lithium superionic argyrodite Li 6 PS 5 Br. *Energy Adv.* **2023**, *2*, 1915−1925.
(38) Lee, S.-Y.; Han, J.-H.; Gong, H.-W.; Ahn, J.; Yi, K.-W.; Whan Cho, Y. Characterization of densification behavior and mechanical properties of solid electrolyte powders for all solid-state batteries. *J. Mater. Chem. A* **2025**, *13*, 6342−6346.
(39) Faka, V.; Alabdali, M.; Lange, M. A.; Zanotto, F. M.; Yildirim, C.; Kanedal, M. D.; Kondek, J.; Hartmann, M.; Maus, O.; Daisenberger, D.; et al. How Particle Size Affects Consolidation Behavior, Strain and Properties of Li6PS5Cl Fast Ionic Conductors. *Adv. Energy Mater.* **2026**, *16* (12), No. e05186.
(40) Gao, X.; Liu, B.; Hu, B.; Ning, Z.; Jolly, D. S.; Zhang, S.; Perera, J.; Bu, J.; Liu, J.; Doerrer, C.; Darnbrough, E.; Armstrong, D.; Grant, P. S.; Bruce, P. G. Solid-state lithium battery cathodes operating at low pressures. *Joule* **2022**, *6*, 636−646.
(41) Zhang, W.; Leichtweiß, T.; Culver, S. P.; Koerver, R.; Das, D.; Weber, D. A.; Zeier, W. G.; Janek, J. The Detrimental Effects of Carbon Additives in Li10GeP2S12-Based Solid-State Batteries. *ACS Applied Materials Interfaces* **2017**, *9*, 35888−35896.
(42) Walther, F.; Randau, S.; Schneider, Y.; Sann, J.; Rohnke, M.; Richter, F. H.; Zeier, W. G.; Janek, J. Influence of Carbon Additives on the Decomposition Pathways in Cathodes of Lithium Thiophosphate-Based All-Solid-State Batteries. *Chem. Mater.* **2020**, *32*, 6123−6136.
(43) Bielefeld, A.; Weber, D. A.; Janek, J. Modeling Effective Ionic Conductivity and Binder Influence in Composite Cathodes for All-Solid-State Batteries. *ACS Applied Materials Interfaces* **2020**, *12*, 12821−12833.
(44) Froboese, L.; Sichel, J. F. V. D.; Loellhoeffel, T.; Helmers, L.; Kwade, A. Effect of Microstructure on the Ionic Conductivity of an All Solid-State Battery Electrode. *J. Electrochem. Soc.* **2019**, *166*, A318−A328.
(45) Strauss, F.; Bartsch, T.; De Biasi, L.; Kim, A.-Y.; Janek, J.; Hartmann, P.; Brezesinski, T. Impact of Cathode Material Particle Size on the Capacity of Bulk-Type All-Solid-State Batteries. *ACS Energy Lett.* **2018**, *3*, 992−996.
(46) Minnmann, P.; Quillman, L.; Burkhardt, S.; Richter, F. H.; Janek, J. Editors' Choice—Quantifying the Impact of Charge Transport Bottlenecks in Composite Cathodes of All-Solid-State Batteries. *J. Electrochem. Soc.* **2021**, *168*, 040537.
(47) Schlautmann, E.; Weiß, A.; Maus, O.; Ketter, L.; Rana, M.; Puls, S.; Nickel, V.; Gabbey, C.; Hartnig, C.; Bielefeld, A.; et al. Impact of the Solid Electrolyte Particle Size Distribution in Sulfide-Based Solid-State Battery Composites. *Adv. Energy Mater.* **2023**, *13*, 2302309.
(48) Bielefeld, A.; Weber, D. A.; Rueß, R.; Glavas, V.; Janek, J. Influence of Lithium Ion Kinetics, Particle Morphology and Voids on the Electrochemical Performance of Composite Cathodes for All-Solid-State Batteries. *J. Electrochem. Soc.* **2022**, *169*, 020539.
(49) Bae Song, Y.; Kwak, H.; Cho, W.; Kim, K. S.; Seok Jung, Y.; Park, K.-H. Electrochemo-mechanical effects as a critical design factor for all-solid-state batteries. *Curr. Opin. Solid State Mater. Sci.* **2022**, *26*, 100977.
(50) Kirillov, A.; Mintun, E.; Ravi, N.; Mao, H.; Rolland, C.; Gustafson, L.; Xiao, T.; Whitehead, S.; Berg, A. C.; Lo, W.-Y.; et al. Segment Anything. *arXiv*, **2023**.
(51) Van Der Walt, S.; Schönberger, J. L.; Nunez-Iglesias, J.; Boulogne, F.; Warner, J. D.; Yager, N.; Gouillart, E.; Yu, T. scikit-image: Image processing in Python. *PeerJ.* **2014**, *2*, No. e453.
(52) Kissel, M.; Schosland, M.; Töws, J.; Kalita, D.; Schneider, Y.; Kessler-Kühn, J.; Schröder, S.; Schubert, J.; Frankenberg, F.; Kwade, A.; et al. Quantifying the Impact of Cathode Composite Mixing Quality on Active Mass Utilization and Reproducibility of Solid-State Battery Cells. *Adv. Energy Mater.* **2025**, *15* (27), 2405405.
(53) Zhang, W.; Weber, D. A.; Weigand, H.; Arlt, T.; Manke, I.; Schröder, D.; Koerver, R.; Leichtweiss, T.; Hartmann, P.; Zeier, W. G.; Janek, J. Interfacial Processes and Influence of Composite Cathode Microstructure Controlling the Performance of All-Solid-State Lithium Batteries. *ACS Appl. Mater. Interfaces* **2017**, *9*, 17835−17845.
(54) Maus, O.; Lange, M. A.; Frankenberg, F.; Stainer, F.; Faka, V.; Schlautmann, E.; Rosenbach, C.; Jodlbauer, A.; Schubert, J.; Janek, J.; et al. Influence of Post-Synthesis Processing on the Structure, Transport, and Performance of the Solid Electrolyte Li5.5PS4.5Cl1.5 in All-Solid-State Batteries. *Adv. Energy Mater.* **2024**, *15*, 2403291.
(55) Wang, Y.; Hao, H.; Naik, K. G.; Vishnugopi, B. S.; Fincher, C. D.; Yan, Q.; Raj, V.; Celio, H.; Yang, G.; Fang, H.; et al. Mechanical Milling − Induced Microstructure Changes in Argyrodite LPSCl Solid-State Electrolyte Critically Affect Electrochemical Stability. *Adv. Energy Mater.* **2024**, *14* (23), 2304530.
(56) Sakuda, A.; Hayashi, A.; Tatsumisago, M. Sulfide Solid Electrolyte with Favorable Mechanical Property for All-Solid-State Lithium Battery. *Sci. Rep.* **2013**, *3*, 2261.
(57) Ates, T.; Neumann, A.; Danner, T.; Latz, A.; Zarrabeitia, M.; Stepien, D.; Varzi, A.; Passerini, S. Elucidating the Role of Microstructure in Thiophosphate Electrolytes − a Combined Experimental and Theoretical Study of β -Li 3 PS 4. *Adv. Sci.* **2022**, *9* (18), 2105234.
(58) Famprikis, T.; Kudu, Ö. U.; Dawson, J. A.; Canepa, P.; Fauth, F.; Suard, E.; Zbiri, M.; Dambournet, D.; Borkiewicz, O. J.; Bouyanfif, H.; Emge, S. P.; Cretu, S.; Chotard, J.-N.; Grey, C. P.; Zeier, W. G.; Islam, M. S.; Masquelier, C. Under Pressure: Mechanochemical Effects on Structure and Ion Conduction in the Sodium-Ion Solid Electrolyte Na_3PS_4. *J. Am. Chem. Soc.* **2020**, *142*, 18422−18436.
(59) Korte, C.; Keppner, J.; Peters, A.; Schichtel, N.; Aydin, H.; Janek, J. Coherency strain and its effect on ionic conductivity and diffusion in solid electrolytes − an improved model for nanocrystalline thin films and a review of experimental data. *Phys. Chem. Chem. Phys.* **2014**, *16*, 24575−24591.
(60) Kuo, J. J.; Kang, S. D.; Chueh, W. C. Contact Resistance of Carbon−Li x (Ni,Mn,Co)O 2 Interfaces. *Adv. Energy Mater.* **2022**, *12* (31), 2201114.
(61) Siroma, Z.; Fujiwara, N.; Yamazaki, S.; Asahi, M.; Nagai, T.; Ioroi, T. Mathematical solutions of comprehensive variations of a transmission-line model of the theoretical impedance of porous electrodes. *Electrochim. Acta* **2015**, *160*, 313−322.
(62) Siroma, Z.; Sato, T.; Takeuchi, T.; Nagai, R.; Ota, A.; Ioroi, T. AC impedance analysis of ionic and electronic conductivities in electrode mixture layers for an all-solid-state lithium-ion battery. *J. Power Sources* **2016**, *316*, 215−223.
(63) Miß, V.; Seus, S.; Marx, A.; Steyer, E. D.; Mereacre, V.; Binder, J. R.; Roling, B. Influence of Pressure, Particle Morphology, Coating, and Heat Treatment on the Effective Electronic Conductivity of Cathode Active Materials for All-Solid-State Batteries. *ACS Mater. Lett.* **2025**, *7*, 2262−2269.
(64) Aktekin, B.; Sedykh, A. E.; Müller-Buschbaum, K.; Henss, A.; Janek, J. The Formation of Residual Lithium Compounds on Ni-Rich NCM Oxides: Their Impact on the Electrochemical Performance of Sulfide-Based ASSBs. *Adv. Funct. Mater.* **2024**, *34* (21), 2313252.
(65) Culver, S. P.; Koerver, R.; Zeier, W. G.; Janek, J. On the Functionality of Coatings for Cathode Active Materials in Thiophosphate-Based All-Solid-State Batteries. *Adv. Energy Mater.* **2019**, *9*, 1900626.
(66) Ohashi, A.; Kodama, M.; Xueying, S.; Hori, S.; Suzuki, K.; Kanno, R.; Hirai, S. Stress distribution in the composite electrodes of sulfide all-solid-state lithium-ion batteries. *J. Power Sources* **2020**, *470*, 228437.

https://doi.org/10.1021/acselectrochem.6c00144
ACS Electrochem. 2026, 2, 1583−1597

(67) Dai, T.; Wu, S.; Lu, Y.; Yang, Y.; Liu, Y.; Chang, C.; Rong, X.; Xiao, R.; Zhao, J.; Liu, Y.; Wang, W.; Chen, L.; Hu, Y.-S. Inorganic glass electrolytes with polymer-like viscoelasticity. *Nat. Energy* **2023**, *8*, 1221−1228.
(68) Wang, G.; Zhang, S.; Wu, H.; Zheng, M.; Zhao, C.; Liang, J.; Zhou, L.; Yue, J.; Zhu, X.; Xu, Y.; et al. Oxychloride Polyanion Clustered Solid-State Electrolytes via Hydrate-Assisted Synthesis for All-Solid-State Batteries. *Adv. Mater.* **2025**, *37*, 2410402.
(69) You, I.; Singh, B.; Cui, M.; Goward, G.; Qian, L.; Arthur, Z.; King, G.; Nazar, L. F. A facile route to plastic inorganic electrolytes for all-solid state batteries based on molecular design. *Energy Environ. Sci.* **2025**, *18*, 478−491.
(70) Randau, S.; Walther, F.; Neumann, A.; Schneider, Y.; Negi, R. S.; Mogwitz, B.; Sann, J.; Becker-Steinberger, K.; Danner, T.; Hein, S.; Latz, A.; Richter, F. H.; Janek, J. On the Additive Microstructure in Composite Cathodes and Alumina-Coated Carbon Microwires for Improved All-Solid-State Batteries. *Chem. Mater.* **2021**, *33*, 1380−1393.

https://doi.org/10.1021/acselectrochem.6c00144
ACS Electrochem. 2026, 2, 1583−1597